A&A 480, 589–597 (2008)
DOI: 10.1051/0004-6361:20079214

Astronomy & Astrophysics

The point spread function in Lucky Imaging and variations in seeing on short timescales

J. E. Baldwin[1], P. J. Warner[1], and C. D. Mackay[2]

[1] Cavendish Laboratory, Madingley Rd, Cambridge CB3 0HE, UK
e-mail: [jeb;pjw]@mrao.cam.ac.uk
[2] Institute of Astronomy, Madingley Rd, Cambridge CB3 0HE, UK
e-mail: cdm@ast.cam.ac.uk

Received 7 December 2007 / Accepted 22 December 2007

ABSTRACT

Aims. We investigate the properties of astronomical images made by combining the best images selected from a sequence of short-exposure frames (Lucky Imaging); we assess the match between modelling and observation and discover what variations in seeing occur on very short timescales.
Methods. Numerical simulations of a random phase-changing screen passing across a telescope aperture with ideal optics are used to determine the expected point spread function and isoplanatic properties for a range of seeing conditions for comparison with observations.
Results. All the model images comprise a diffraction-limited core with Strehl ratios from 0.05–0.5 and an underlying broad disk. The isoplanatic patch sizes are large and coherence times long. The observations are a close match to the models in most respects. Large variations in seeing occur on temporal scales as short as 0.2 s and spatial scales as small as 1 m.

Key words. atmospheric effects – techniques: high angular resolution

1. Introduction

We have used the term Lucky Imaging in several earlier papers (Baldwin et al. 2001; Tubbs et al. 2002; Mackay et al. 2003; Law et al. 2006) to describe the technique of improving angular resolution in astronomical images by combining images with the best Strehl ratios selected from a sequence of short-exposure frames using recentring on the brightest speckle. This follows the original usage by Fried (1978) applied to the selection of the single best image from a sequence. Law et al. (2006) presented observations made with the 2.5 m Nordic Optical Telescope (NOT) at wavelengths close to 800 nm giving a quantitative assessment of the improved resolution obtained in practice. The main conclusions were:

1. The full width to half maximum (FWHM) of images was improved, relative to conventional imaging, by a factor of about 2 if all of the data were recentred and by a factor up to 4 if the best 1% of data were selected for recentring.
2. These factors of improvement in the FWHM applied over a wide range of seeing conditions.
3. The radius of the area of isoplanatism was unexpectedly large, ∼20 arcsec for a reduction in the Strehl ratio by a factor of 2 relative to the value at the centre of the field.
4. Stars as faint as $m = +16$ could be used as reference objects for the selection of frames when using an L3CCD camera with very low readout-noise.
5. The results 3) and 4) implied that the method could be used over about 20% of the sky.

It was noted on several occasions that the mean seeing appeared to change by a large amount on a timescale of ∼1 s but we were not able to distinguish and quantify the changes because of the intrinsic random fluctuations expected in the turbulent atmospheric screen. It was therefore not clear whether the results listed above were a consequence of selecting the moments of favourable fluctuations in a period of constant mean seeing or whether in practice the selection was for periods of better average seeing. For instance, the large isoplanatic patch size might have occurred only during periods when the mean seeing was exceptionally good. This distinction may seem of little importance to an astronomer whose sole interest is in obtaining images with better resolution; but it is essential to an understanding of the application of the technique to telescopes of differing sizes and to the basic question of whether the behaviour of seeing conforms to that expected from the models in general use. A second unanswered question was by how much the small errors in figuring of the NOT mirrors reduced the performance of Lucky Imaging relative to that potentially achievable with ideal optics. In this paper we explore these questions using simulations of a random phase screen moving past the telescope aperture. In Sect. 2 we describe the model and in subsequent sections we attempt to answer the following questions:

1. What are the expected properties of Lucky images made with ideal telescope optics under conditions of constant mean seeing?
2. Are the conclusions from the NOT observations consistent with a constant value of the seeing during one sequence of frames?
3. What is the best measure of seeing on short timescales and what variations in seeing on different time-scales can be established from the NOT data?

We comment briefly on the implications of the rapid changes which are found in the NOT data for other techniques of high-resolution imaging and for the model of seeing in common use.

2. Simulations of seeing

Numerical simulations of stellar images observed through a random phase screen were adopted for this discussion. They provide images which can be analysed in exactly the same way as the observational data and they allow estimation of observational parameters which are difficult to extract using the analytic methods employed in many investigations of seeing.

The simulations were made to match the circumstances of the observations made with the 2.5 m Nordic Optical Telescope, mostly with a 20% bandwidth at wavelengths near 800 nm, under seeing conditions ranging from 0.4−1.2 arcsec. Their application is much wider since the properties of the images are determined by the ratio, D/r_0, of the telescope aperture D to the Fried seeing parameter r_0. For instance, they would apply equally to a 4 m aperture at 1.3 μm and an 8 m aperture at 2.2 μm under similar seeing conditions. It is likely that a similarly wide bandwidth will be necessary at most wavelengths to allow the use of faint reference stars. We therefore present the results as a function of D/r_0 in Sect. 3 and convert them to the NOT parameters for comparison with the observations in Sect. 4. The range of values of D/r_0 in these simulations and observations is approximately 6−18. This range was already identified by earlier authors (Hecquet & Coupinot 1984) as being one in which significant improvements in angular resolution could be achieved by selection and recentring of images.

A 2-dimensional random phase screen was generated within a 2048 × 2048 pixel array, based on the code developed by Buscher (1988). For each screen the amplitude $a(k)$ for each cosine and sine component of spatial frequency k were chosen as independent Gaussian random variables with zero mean and variance $\langle a^2(k)\rangle \propto k^{-11/3}$. The diameter, D, of the telescope aperture was chosen to be 56 pixels. Then, in the comparison with the NOT observations, the largest scale of turbulence in the simulation is ∼100 m and the smallest ∼0.09 m. The consequent truncations of the Kolmogorov spectrum have no significant effect on the results. The largest scales provide only tip-tilt variation of phase across the 2.5 m aperture and are therefore removed in the shift-and-add process. 100 m is, in any case, as large as the outer scale of turbulence believed to exist for most sites. The power missing at the shortest scales is too small to affect the results except for seeing poorer than we have used in these simulations. We have not explored the effects of alternative slopes in the power spectrum of turbulence but draw attention in Sects. 3.1 and 4 to observational aspects of short-exposure images which reveal it.

Images of stars were generated by taking a 512 × 512 subarray centred on the telescope aperture with unit amplitude and the corresponding phases within the aperture and zero amplitude outside. The square of the Fourier transform of this 2-dimensional array gives one instantaneous image. Several checks were made on the overall normalisation of the process, first by averaging the images from a large number of phase screens, confirming that the expected seeing disk was generated. Other checks were provided by the tilt-corrected mean phase variance over the telescope aperture discussed in Sect. 3.1. It was to allow these comparisons that the effect of secondary mirror blockage was not included in the simulations; for most telescopes the effects are small. Two additions to the model were made to meet the circumstances of the observations and their analysis as closely as possible. Images simulating a 20% optical bandwidth were constructed by calculating the image for 11 uniformly spaced wavelengths, λ, across the band, the phases in the screen being scaled as λ^{-1}. Since the angular scale of the images on the sky is proportional to λ, averaging of the images also required linear interpolation of each image to a standard angular scale. The second feature was to move the aperture across the screen from the lower left to the upper right corner to create a sequence of 664 successive instantaneous images corresponding to a "frozen" turbulent screen carried by the wind crossing the telescope aperture. Comparisons could then be made with temporal and isoplanatic aspects of the observations. The spatial interval between successive images corresponded to shifts of $0.07575D$, or 0.187 m for the NOT comparison, which is adequate sampling for all aspects of the analysis.

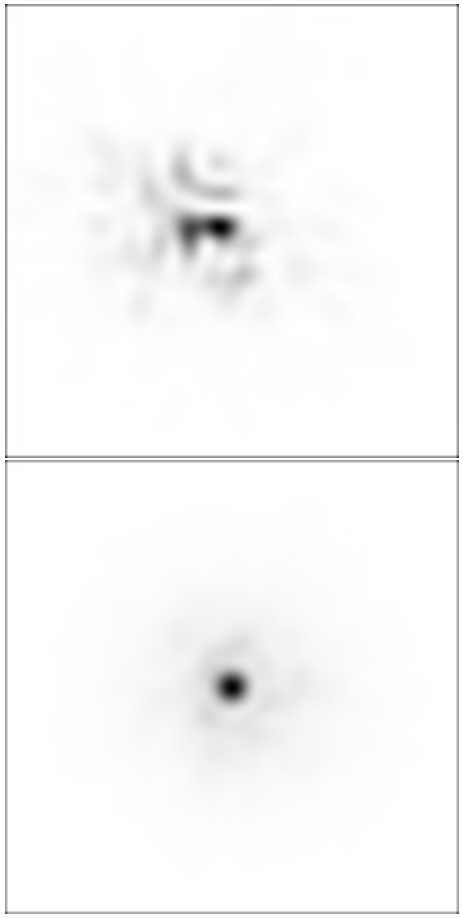

Fig. 1. a) One instantaneous image; D/r_0 = 8.3, Strehl ratio 0.16. **b)** Average of best 10% of images; D/r_0 = 8.3, Strehl ratio 0.19.

This procedure was repeated for a number, typically 8, of different phase screens for each value of D/r_0. The residual statistical fluctuations in the results presented here due to the finite number of frames are small but may account for some of the differences between the curves in Figs. 6 and 7.

Figure 1a shows a typical short-exposure image for D/r_0 = 8.3. It has a Strehl ratio of 0.16. 10% of the images in this sequence have higher Strehl ratios. The image formed by shift-and-add on these 10% is shown in Fig. 1b. Much of the speckle is averaged out in this image which corresponds to the analysis of about 10 s of data for the NOT parameters.

3. Analysis of the simulated images

3.1. The radial profile

Each image in a sequence of 664 was analysed initially to give a list of parameters including the shifts in position of the peak

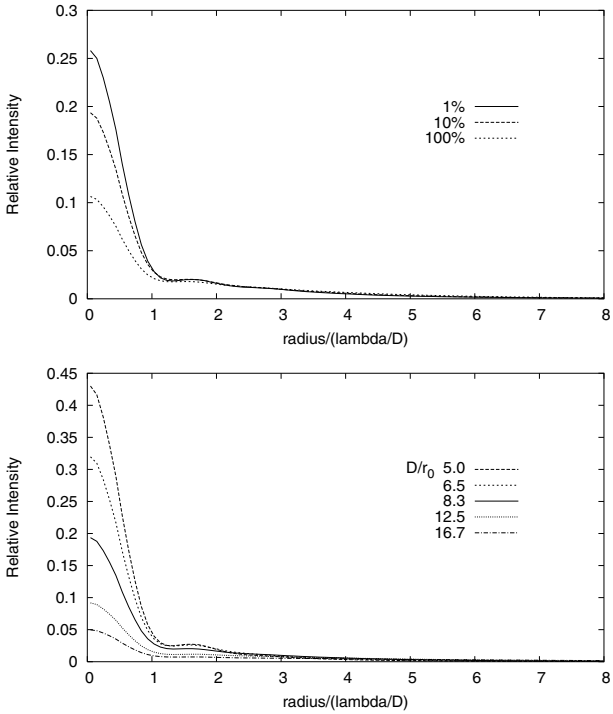

Fig. 2. Mean radial profiles of images **a)** $D/r_0 = 8.3; 1, 10, 100\%$ selection. **b)** $D/r_0 = 5, 6.5, 8.3, 12.5, 16.7$; 10% selection. The intensity scale has been normalised so that the peak value for each profile is the Strehl ratio of that image.

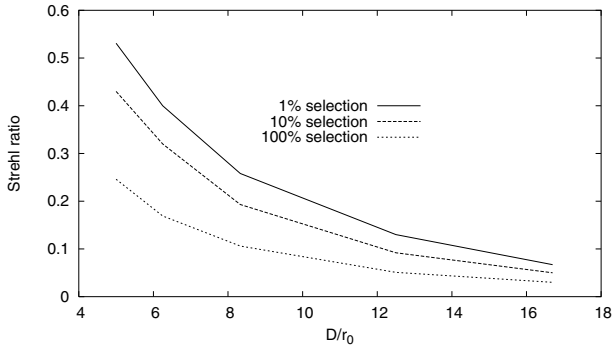

Fig. 3. Strehl ratios for a range of D/r_0 and % selection.

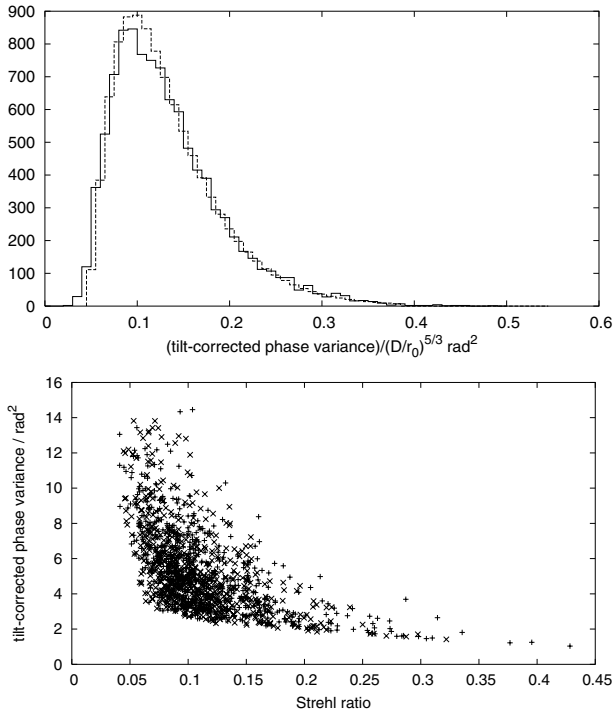

Fig. 4. **a)** Full line: histogram of tilt-corrected phase variances for 10 000 independent phase screens. Dashed line: theoretical distribution for Zernike modes $Z_4 - Z_{10} + 0.04$ (to represent all higher modes). **b)** Phase variances and Strehl ratios for a sequence of frames with $D/r_0 = 8.3$.

pixel and the centroid relative to their undeviated values, the Strehl ratio and the full widths enclosing 30, 50 and 70% of the flux. Images selected by their Strehl ratios could then be combined using shift-and-add to give resulting images with a range of percentages of selection. The radial distribution of flux in each combined image was obtained by integration in narrow annuli centred on the peak pixel of the image. The mean radial profiles for a range of percentage selection for $D/r_0 = 8.3$ and for a range of D/r_0 for 10% selection are shown in Fig. 2, all the curves being plotted on the same intensity scale to allow direct comparison of the Strehl ratios of the images. In each case the main features are a central peak corresponding to the ideal diffraction-limited response of the aperture D superimposed on a much broader feature whose dimensions are roughly similar to those of the normal seeing disk. In these respects the images resemble those seen in analysis of observations with the NOT (see Fig. 4 of Law et al. (2006) and Sect. 3.3 of this paper). As noted in the earlier paper, they are also similar to those seen in partially corrected images using adaptive optics. Figure 3 summarises the results obtained for the Strehl ratios of images for a wide range of D/r_0 and percentage selection.

We now examine some of the properties of the phase fluctuations which are responsible for the variations of the Strehl ratios. The distribution of the tilt-corrected phase variance, $\langle\phi^2\rangle$, across the aperture for 10 000 independent phase screens in these simulations is shown in Fig. 4a. Its mean value is $0.133(D/r_0)^{5/3}$. This is in good agreement with the coefficient of 0.134 given by Noll (1976). The value here is expected to be marginally smaller because of the truncation of the model turbulent spectrum at small and large scales but in any case the agreement is within the expected statistical error. The highest Strehl ratios on the plot in Fig. 3 are a good fit to the approximate formula

$$\text{Strehl ratio } S = \exp(-\langle\phi^2\rangle). \quad (1)$$

For instance, the 1% of values with smallest phase variance in the histogram have a mean value of $0.045(D/r_0)^{5/3}$, giving an expected Strehl ratio of 0.518 for $D/r_0 = 5$. Notice that the steep slope of the $\langle\phi^2\rangle$ histogram for small values of $\langle\phi^2\rangle$ implies that there is only a small penalty in achievable Strehl ratio for selecting as much as 10% of the data, as Fig. 3 confirms. In some cases it may be desirable to use an even larger percentage of the data. The consequent reduction in Strehl ratio has to be balanced against improvement in both the signal-to-noise ratio in the combined image and averaging of the residual speckle in the outer parts of the point spread function. It provides flexibility in matching the analysis to the astronomical requirements of the programme.

It is of interest to examine the contributions to the wide spread of values displayed in Fig. 4a. The mean for the whole histogram is $0.133(D/r_0)^{5/3}$. The corresponding coefficient for the first three Zernike modes after tip-tilt correction, $(Z_4 - Z_6)$, is 0.069, and 0.094 if the first seven modes, $(Z_4 - Z_{10})$, are included

(Noll 1976). All the higher modes contribute a mean of only 0.04 to the total. The amplitudes of the Zernike modes are Gaussian random variables and for any such variable x with variance σ^2, the probability distribution of x^2 has a mean value of σ^2 and a variance $2\sigma^4$. Hence the high order modes make an extremely small contribution (1.5%) to the spread of phase variance, whilst 90% is provided by the modes ($Z_4 - Z_6$). The dotted histogram shows the effect of calculating the full probability distribution for the Zernike terms ($Z_4 - Z_{10}$) and taking a delta function at 0.04 to represent the probability distribution of all the higher terms.

Important consequences of this are that the mean value of $0.04(D/r_0)^{5/3}$ of the phase variance for the higher order terms is the lower limit to the phase variance histogram and hence sets an upper limit to the Strehl ratio of the images. Variations in the distribution of power between the higher modes will alter the speckle pattern in the outer parts of images but exert almost no influence on variations in the Strehl ratios and hence no influence on the selection of Lucky images. The few lowest order Zernike modes determine a large correlation length for the Strehl ratios as the screen is moved past the telescope aperture, resulting in large isoplanatic patch sizes (Sect. 3.2) and correspondingly long correlation times (Sect. 3.3).

An example of the Strehl ratios of a set of instantaneous images and their associated tilt-corrected phase variances for $D/r_0 = 8.3$ is shown in Fig. 4b. As expected, the highest Strehl ratios correspond to the smallest residual phase variances across the aperture and there is a general decrease in Strehl ratio with increasing phase variance; but some of the higher Strehl ratios are associated with images in which the phase variance is large. These are examples of a behaviour which, in the extreme case of a square wave phase variation of one wavelength peak-to-peak amplitude, would give a Strehl ratio of unity. It illustrates that the images obtained by selection for Strehl ratio in Lucky Imaging are not identical to those obtained by selection for residual phase variance; nor will they be identical to those given by partially-corrected adaptive optics in which the aim has been to minimise the residual phase variance.

The outer parts of the radial profiles can be seen best in the logarithmic plots, Figs. 5a and b, with the same percentage selection and D/r_0 parameters as in Fig. 2. A profile for a conventional long-exposure image is included for comparison. A feature of all the profiles is the constant slope of the curves close to $-11/3$ in the outermost parts. It can be understood in terms of a simplified one-dimensional model. For a sinusoidal spatial variation of phase, ϕ, in the screen

$$\phi = \phi_0 \cos(kx), \tag{2}$$

a plane wave of unit amplitude transmitted through the turbulent screen becomes

$$\begin{aligned} \exp(i\phi) &= \cos(\phi_0 \cos kx) + i \sin(\phi_0 \cos kx) \\ &= 1 + i\phi_0 \cos(kx) \quad \text{if } \phi_0 \ll 1 \text{ radian}, \end{aligned} \tag{3}$$

a condition which applies for all the higher spatial frequencies. The transmitted radiation comprises an undeviated beam and scattered beams with amplitude $\propto\phi_0$ at angles

$$\theta = \pm(k/2\pi\lambda). \tag{4}$$

Each spatial frequency is associated with a single angle of scattering proportional to k and its intensity is proportional to ϕ_0^2. Hence the power law index of the radial intensity profile in the outer parts of the image is the same as that of the power spectrum of phase fluctuations in the simulations, $-11/3$ for the Kolmogorov spectrum. It provides a simple method for rapid measurement of that slope. A practical example is discussed in Sect. 4. This result has been derived previously in the context of extra-solar planet detection (Perrin et al. 2003) in the uncorrected halos of images of very high Strehl ratio from adaptive optics.

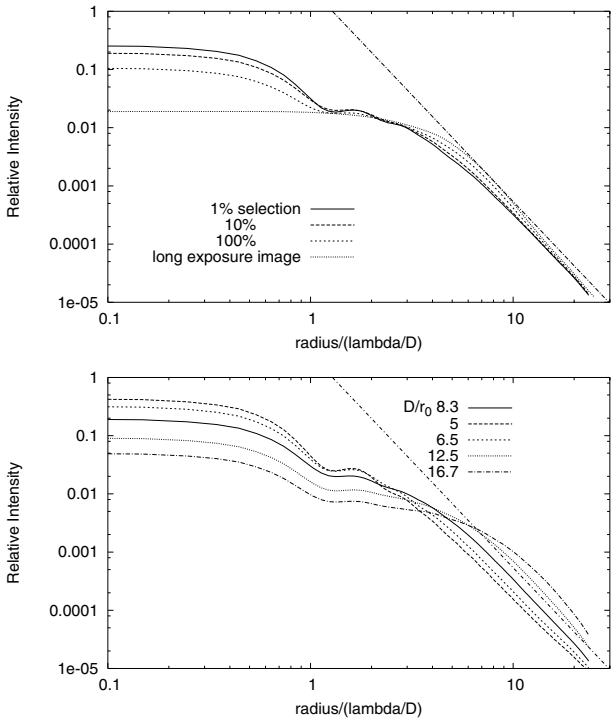

Fig. 5. Mean radial profiles of images **a)** $D/r_0 = 8.3; 1, 10, 100\%$ selection. **b)** $D/r_0 = 5, 6.5, 8.3, 12.5, 16.7; 10\%$ selection. A line of slope $-11/3$ on each plot is for comparison purposes. The intensity scale has been normalised so that the peak value for each curve is the Strehl ratio of that image.

For small spatial frequencies, ϕ_0 may be >1 radian, say n radians. The scattered beams lie as before at $\theta = \pm(k/2\pi\lambda)$, and also its harmonics out to $\theta = \pm n(k/2\pi\lambda)$ but falling very rapidly in amplitude at larger angles. The small spatial frequencies thus make no direct contribution to the distribution of intensity at large angles. There are in addition some cross-product terms between the large and small spatial frequencies, k_l and k_s, giving contributions at angles

$$\theta = \pm((k_l \pm k_s)/2\pi\lambda). \tag{5}$$

These terms add a small amount to the radial intensity at large radii. The amount is negligible for 1% selection of images for all the values of D/r_0 discussed here, since these have only small phase variances associated with the low spatial frequencies. It increases slightly with the amplitude of the low spatial frequency terms and hence also with the percentage of images selected. These terms introduce some smoothing in angle of the scattered power spectrum but do not change the value of its slope in a region where it is constant.

3.2. Isoplanatism

The discussion up to this point has emphasized the properties of the reference star images. The key issue for the use of Lucky imaging as a generally applicable technique is whether target objects lie within the region of isoplanatism of the reference star. For a single frozen screen moved relative to the telescope

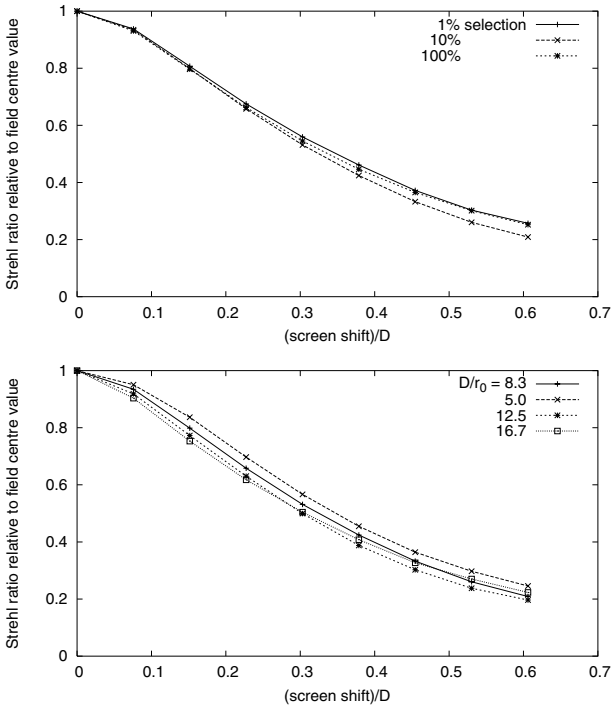

Fig. 6. Isoplanatic effect of decrease in Strehl ratio as a function of shift in the screen **a)** $D/r_0 = 8.3; 1, 10, 100\%$ selection **b)** $D/r_0 = 5, 8.3, 12.5, 16.7, 10\%$ selection.

aperture, the sequence of images can be interpreted either as a time sequence for any chosen wind speed (Sect. 3.3) or to analyse the isoplanatic behaviour of the model. As discussed above, the image of the star chosen as the reference object is analysed by choosing the percentage of frames to be included, checking whether a particular frame should be included and, if so, adding its contribution to the combined image with its measured positional shifts. A star displaced from the centre of the field by an angle θ will be seen by the telescope through a patch of the screen displaced by a distance $h\theta$, where h is the assumed height of the screen. Thus, to construct the expected image at an angle θ from the reference star, images are taken from the sequence displaced by $h\theta$ from each of the selected reference star images and combined as before but using the same positional shifts as are used for the reference star. The net effect of these changes is that the images of stars at a distance from the reference have lower Strehl ratios, falling progressively with distance. Figures 6a and b show these reductions for several values of D/r_0 and for three differing percentages of selection. The Strehl ratios fall by a factor of two relative to the value at the centre of the field for a displacement of the screen $\Delta d = 0.33D$ and a corresponding angular radius $\Delta\theta_{1/2} = 0.33D/h$. The effect is only weakly dependent on the percentage selection of images or on the ratio D/r_0 over the range of values considered here, some of the differences between the curves being due to statistical fluctuations from the finite simulations. The independence of seeing is expected following the discussion in Sect. 3.1 where it was shown that the spatial scale of variations in Strehl ratios arises from the relative weights of the lowest Zernike modes and hence depends only on the aperture size D and not on the seeing. It will therefore also be independent of wavelength.

This is of practical importance, since small changes in the seeing during an observing run will not affect the factors, as a function of radius, needed to correct the image intensities to a uniform scale over the whole field. If the field of view is very

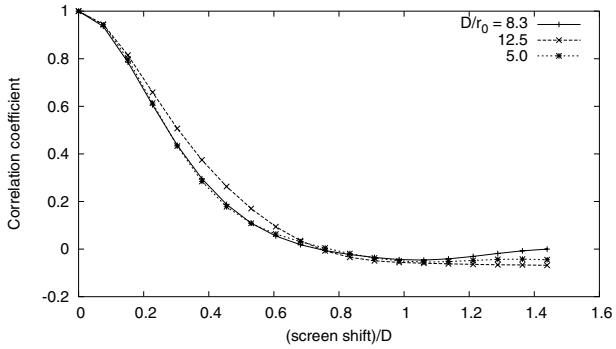

Fig. 7. Autocorrelation function of Strehl ratios as a function of shift of the screen for $D/r_0 = 5, 8.3, 12.5$.

large, so that several reference stars are available, the same analysis will apply for each of these stars giving the same isoplanatic response with radius from that star even though different frames from the sequence are being selected for each reference object.

The atmospheric fluctuations are not in general confined to a layer at a single height. The shape of the curves in Fig. 6 will be affected by the range of values of h present but no overall qualitative change in isoplanaticity is expected, since the same argument regarding the correlation scale applies for all the layers. This conclusion may appear to conflict with the results of Roddier et al. (1982) in their analysis of the isoplanatic patch size in speckle interferometry. They obtain an isoplanatic angular size $\sim D/h$ for a single thin turbulent layer but $\sim r_0/\Delta h$ for a thick layer of thickness Δh. The difference arises from their assumption of a large value of D/r_0 in their application. The Lucky Imaging case, where D/r_0 is small, differs by the image being dominated by a single bright speckle in all the cases considered where selection by Strehl ratio is employed (see Fig. 2).

3.3. Wind speed and optimum exposure times

An important factor in Lucky observations is the choice of exposure time for each frame. For good sensitivity it must be as long as possible without incurring blurring of the images. The simulations used for the isoplanatic patch in Sect. 3.2 give a direct measure of this, since a shift in the screen corresponds to a time interval for any given wind speed. So the effect of a finite integration time on the Strehl ratio of the best images can be deduced by smoothing the curve in Fig. 6 over the appropriate interval. Averaging over a shift of the screen of $\Delta d = \pm 0.15D$ gives an acceptably small reduction in Strehl ratio of 7%, the reduction increasing roughly as the square of the integration time for longer integrations. For the NOT observations this corresponds to an integration time of 75 ms for an assumed wind speed of 10 m s^{-1}. It corresponds well with those found to be satisfactory in practice.

A measure of the wind speed V can be obtained straightforwardly from the time variation of the Strehl ratios. Figure 7 shows the autocorrelation function of the Strehl ratios of a sequence of images for three values of D/r_0 as a function of the distance moved by the screen. The autocorrelation function is independent of the seeing, for the same reasons as discussed for isoplanatism. It falls to 0.5 for values of displacement of about $\Delta d = 0.26D$ and a corresponding time interval $\Delta t_{1/2} = 0.26D/V$.

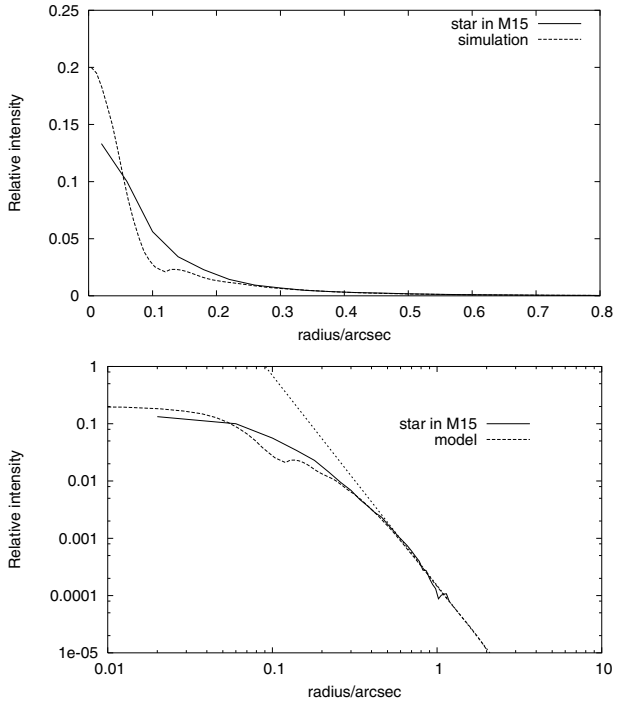

Fig. 8. a) Radial profiles of a star in M15 and simulated image for the same seeing conditions. **b)** Logarithmic plot with line of slope −11/3 added for comparison purposes.

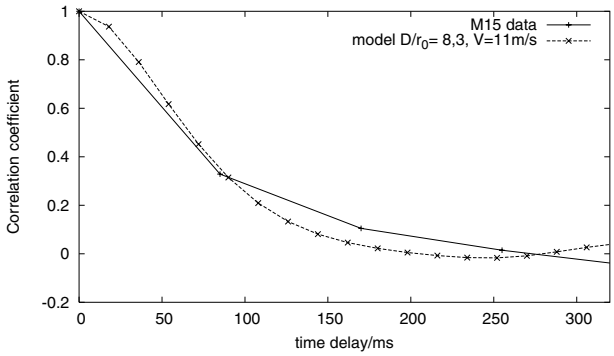

Fig. 9. Autocorrelation function of Strehl ratios: $D/r_0 = 8.3$ model with $V = 11$ m s^{-1} compared with M15 data.

4. Comparison with NOT observations

The results of Sect. 3 can be scaled to the NOT observations using the appropriate value for D/r_0. For 0.6 arcsec seeing at 820 nm, $r_0 = 0.30$ m giving $D/r_0 = 8.3$ for the 2.5 m NOT aperture. Data taken under these conditions are compared with the theoretical profiles from the simulations in Fig. 8. The simulations were made with a pixel scale of 7.2 mas, whilst the actual observations were made with 40 mas pixels on a star separated from the reference by 2 arcsec and with an exposure time of 85 ms. The pixel size affects both the precision of centring the reference star and blurs the profile of the target star. Photon noise in the reference star response must also be considered but is not significant in this example. These factors have been taken into account in generating the curve for $D/r_0 = 8.3$, which is the best estimate of what would be expected in practice. The observed radial profile differs in having a broader central peak and a correspondingly lower Strehl ratio. However, the total flux in the central peak is the same to within 15% in the two cases. The reason for the broadening of the peak is unknown, but the effect is typical of all the data taken in 2003 and 2004 on the NOT. A possible reason is that it is due to residual errors in the mirror figure which are too large to be corrected fully by atmospheric fluctuations. It would not be suprising given that the specification for the primary mirror at the time of construction was that 80 percent of the energy should lie within a circle of 0.4 arcsec diameter. We note however that some of the data in the original Lucky observations in 2001 (Baldwin et al. 2001) did give a central peak in the image which was very close to the diffraction limit. The outer part of the radial profile (Fig. 8), corresponding to spatial scales in the turbulence $\leq(D/4)$, or 0.6 m for the NOT, matches those of the simulations very closely and confirms that the actual slope of the turbulence power spectrum was close to −11/3. A comparison of the rms motions of the image centroid with those in the simulations showed that this slope was maintained at least up to spatial scales as large as 2.5 m.

As discussed in Sect. 3.2, comparison of the isoplanatic patch simulations with the observational data provides a direct estimate of the effective height of the turbulent layer. Values of 17−30 arcsec radius were found by Law et al. (2006) in the NOT observations. With $D = 2.5$ m these give heights for the layer ranging from 5−10 km. We have no independent evidence of the height of the turbulence during NOT observations but these values lie well within the range commonly measured, suggesting that this technique is a useful addition to existing methods of measuring atmospheric parameters.

An example of the autocorrelation function of the Strehl ratios for one sequence of NOT data is shown in Fig. 9 together with the corresponding curve from simulations scaled to fit, giving a wind speed of 11 m s^{-1}.

The overall conclusion of this comparison of the observations and simulations is that the observed Lucky Imaging behaviour is entirely consistent with assuming a constant value of the seeing parameters and the expected statistical variations within that constraint. It does not exclude the possibility that there are intervals when the mean seeing is poorer, since images from those periods would not be chosen in the selection process.The data provide useful evidence on the effective height and wind speed in the turbulent layer.

5. Variations in seeing

The separate question of whether short-period variations in seeing are present in the data requires a measure of the seeing on a short timescale which is unaffected by the natural fluctuations in a random screen for a constant value of the seeing. We assume in this discussion that "the seeing" can be represented by a single quantity, such as r_0 or the FWHM of a long exposure image. It is evident from the previous analysis that some quantities are poor indicators of the mean seeing in a single short-exposure image. For instance, a very wide range of Strehl ratios arise from a single value of the seeing, making the Strehl ratio of a single frame unreliable as a measure of the seeing. The standard measure of full width to half maximum is also of no value for a single exposure since it will be simply that of the brightest speckle, close to the diffraction-limited value. A more useful quantity can be identified by looking at the integral profile of the images. Figure 10 shows the integral of the flux within a given radius for the images in Figs. 2a and 5a for $D/r_0 = 8.3$ and 1, 10 and 100% selection. As the percentage of enclosed flux is increased, the three curves show a progressively smaller scatter in fractional radius indicating that the best values (1% selection) differ least

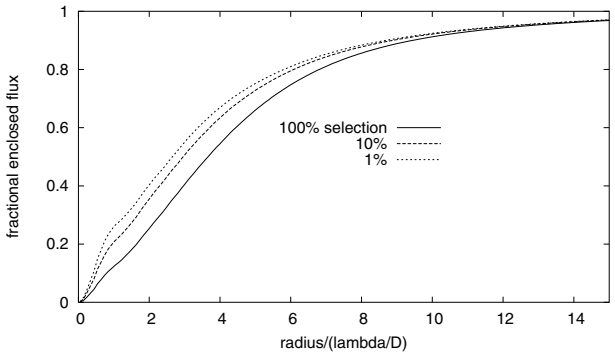

Fig. 10. Integral of flux in image within radius r. $D/r_0 = 8.3; 1, 10$ and 100% selection.

Table 1. Full width 70% enclosed flux/(λ/D).

D/r_0	Mean	rms
5.0	6.48	0.68
6.5	8.26	0.87
8.3	10.84	1.04
12.5	16.00	1.25
16.7	20.74	1.52

from the mean (100% selection). This is a direct consequence of the convergence of the curves in Fig. 5a at large radii, which imply that the fraction of the flux not enclosed will be almost independent of the percentage selection. It suggests that the radius enclosing the largest possible fraction of the flux will give the most consistent estimate of the seeing from a single instantaneous image. In practice this has to be balanced against the difficulty in measuring the very low brightness outer parts of the image against a noisy and perhaps uneven background. For the NOT data taken with LuckyCam, which has exceptionally low noise and good baseline stability, the full width enclosing 70% of the flux (fw70pcef) was found to be a good compromise.

Histograms of this quantity for single instantaneous frames in the simulations show good discrimination of the seeing for each of the values of D/r_0. Their means and rms scatter are listed in Table 1, the ratio of the scatter in the estimates to the mean being about 0.1. Note that the values of fw70pcef are typically a factor of about 1.28× larger than λ/r_0, the FWHM of a conventional image. If the instrumental constraints do not allow such a low brightness level in the image to be used, a lower value of the percentage enclosed flux, say 50% or 30%, can be used but with some loss in discrimination of the seeing value. For 30% enclosed flux, the ratio of rms scatter to the mean increases to about 0.2.

A plot of a sequence of values of fw70pcef from the simulations with $D/r_0 = 8.3$ scaled to the NOT parameters with a velocity of the screen of 10.5 m s^{-1} are compared with the same quantity for the best seeing conditions from the NOT observing run in 2003 in Fig. 11. The two plots are extremely similar in both the amplitude and temporal character of the fast fluctuations, showing that the modelling accurately reflects the actual behaviour of the atmospheric fluctuations. There are in addition some slower variations in the mean seeing in the NOT data on timescales of 5−15 s.

Figure 12a shows a longer sequence of data from 2005 with variations by a factor of ∼1.5× on time scales between 10 s and 400 s (note the change of scale on both axes). These are similar to those discussed by Wilson et al. (1999) for the William Herschel Telescope situated about 400 m from the NOT. More

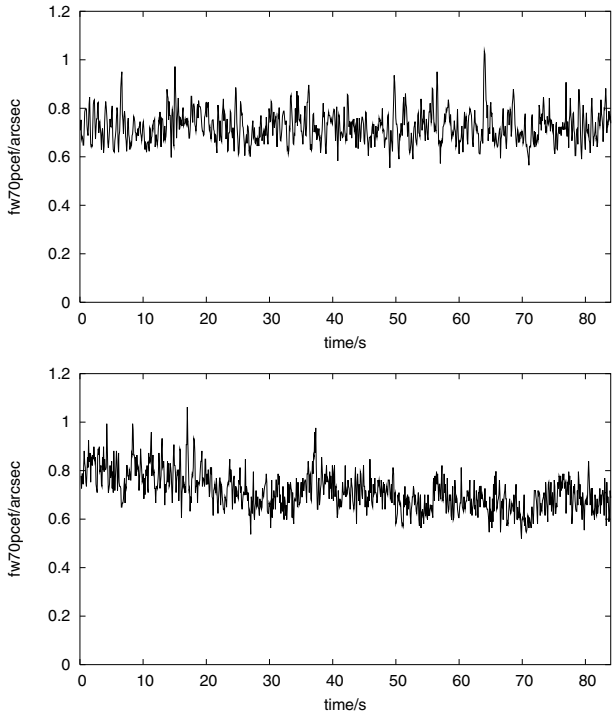

Fig. 11. fw70pcef for a sequence of images **a)** model data with $D/r_0 = 8.3$, $V = 10.5$ m s^{-1}. **b)** Observations of a star in M15.

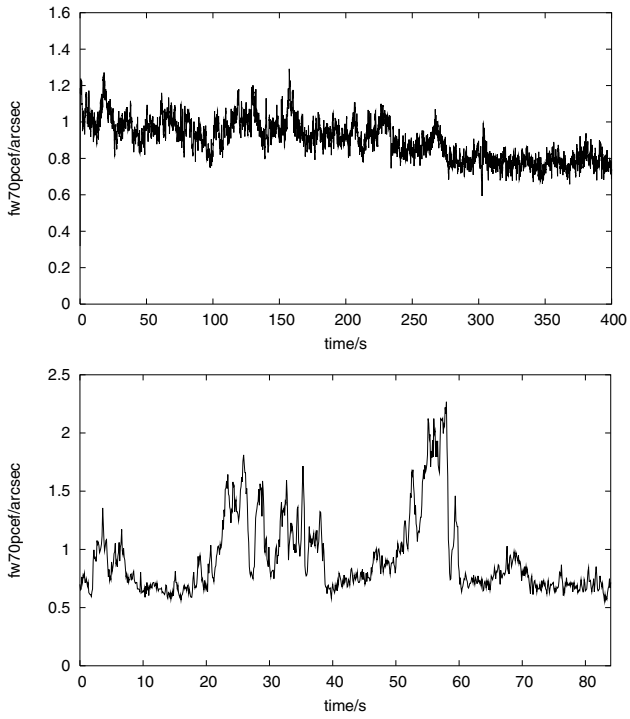

Fig. 12. fw70pcef **a)** from a long run in 2005. **b)** showing large and rapid variations from a run in 2004.

extreme fluctuations are displayed in Fig. 12b, variations in seeing by a factor 3× occurring on timescales as short as 0.2 s.

It raises the question of just how short the transitions can be in the simulations. To test this a mosaic was constructed from two of the phase screens used earlier having $D/r_0 = 8.3$ and 16.7. It comprised alternating stripes of width $1.6D$ from each of the screens with sharp transitions between the stripes. This arrangement is physically unrealistic, giving large

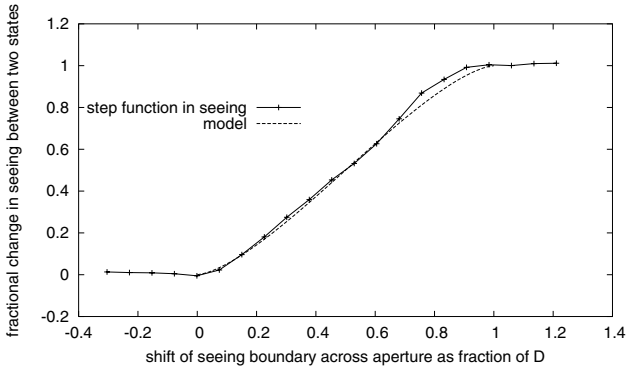

Fig. 13. Change of fw70pcef as step function in seeing crosses the aperture.

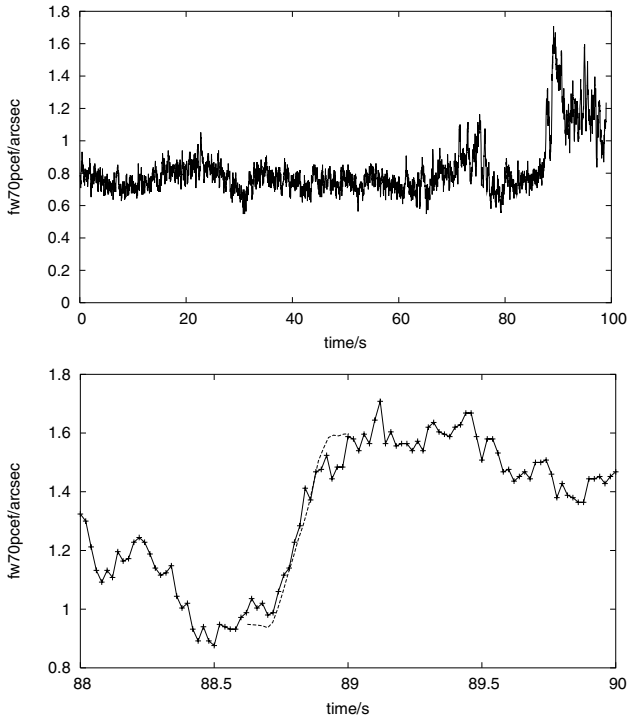

Fig. 14. a) Rapid changes in fw70pcef for a run in 2004. **b)** Comparison of change in fw70pcef with simulation of step change (see text).

discontinuities in phase across the boundaries in some cases, but it represents the limiting case of a seeing change by a factor of two. The behaviour of the quantity fw70pcef as the boundary crosses the aperture is notably smooth. 16 transitions were averaged to reduce the rapid fluctuations in fw70pcef of the type seen in Fig. 11 and the result is plotted in Fig. 13. The main features are well fitted by an approximate model also shown in which the value of fw70pcef is a weighted mean of the two end states, the weights being proportional to the areas of the aperture occupied by each of the two seeing regimes.

A comparison of the simulation with the sharpest transitions in the data requires a knowledge of the effective speed of the screen, derived as discussed in Sect. 3.3 from the autocorrelation function of the sequence of Strehl ratios. That measurement requires a period of constant seeing to avoid the shape of the auto-correlation function being dominated by those seeing changes. NOT data from a run in 2004 (Fig. 14a) shows a period of good and fairly constant seeing followed by a rapid increase in fw70pcef from 0.95 to 1.6 arcsec in about 0.2 s. The variance of the image motion also increases sharply at this point, showing that the change in seeing occurs over a wide range of spatial frequencies. The wind speed derived from the first period was 11 m s^{-1} and this was used to scale the simulation of a step increase in seeing to the NOT parameters. The close agreement with the observations (Fig. 14b) indicates that the change in mean seeing must have been spatially extremely sharp, certainly within a distance of 1 m. This argument depends on the assumption that the motion of the region of poor seeing is travelling at the same speed. If it were in a separate layer travelling at a higher speed, say 20 m s^{-1}, then the constraint on the spatial extent of the transition would be relaxed to about 2 m. However, this possibility would require an even greater contrast between the good and poor seeing in that layer, and seems somewhat unlikely.

On some occasions, variable quality of seeing at the NOT is reported to be associated with wind directions from the E and SE blowing air directly from the caldera. The NOT weather station records for the 2004 observing run show surface wind speeds of 5−10 m s^{-1} in directions between NW and NE, so there is no reason to suspect a local cause for the extreme variations in seeing presented here.

The seeing variations displayed in Figs. 11 and 12a, b were chosen from a very large dataset to be representative of the variations experienced in each of the separate observing runs in 2003, 2005 and 2004 respectively. The range extended from barely perceptible changes occurring over periods of minutes to changes by a factor of 3 or more on timescales down to 0.2 s and included all intermediate types. Figure 12b is of particular interest. The average seeing would be described as moderate yet the periods of good seeing are excellent, with fw70pcef of 0.65 arcsec, equivalent to 0.5 arcsec FWHM of a conventional image. It illustrates how Lucky Imaging can take full advantage of such conditions.

We do not know whether this seeing behaviour is typical of all sites and emphasize the need for appropriate seeing measurements to be made. It represents a significant departure from the model of seeing commonly assumed and would have implications for other high resolution techniques such as Adaptive Optics and Long Baseline Interferometry. For Adaptive Optics the mean seeing conditions may vary significantly on scales smaller than the aperture being corrected, raising difficulties in the optimisation of the modes and timescales for correction. For Long Baseline Interferometry the main effect would be to increase the range of tilt-corrected phase variance across the individual telescope apertures, resulting in a greater probability of very low fringe visibilities. This would make it more difficult to lock the fringe phase, especially in cases where several short baselines are used to enable long integrations on a long baseline.

6. Conclusions

Numerical simulations of the process of Lucky Imaging have been carried out using random phase screens with a Kolmogorov spectrum of turbulence passing across a telescope aperture with ideal optics. Lucky images made by selection and superposition using shift-and-add for a range of 5−16 in D/r_0 all have the same characteristics:

1. A diffraction-limited central peak superposed on a disk with dimensions close to that of the conventional seeing disk. They vary with D/r_0 and percentage selection only in the ratio of the flux in the central peak to that in the disk.

2. The radial profile of the outer parts of the disk has a power law dependence on radius which is the same as that of the power spectrum of the turbulence. It applies for spatial scales smaller than about $D/4$.
3. For a turbulent screen at height h above the telescope, the angular radius at which the Strehl ratio of the image falls to half of that at the field centre is given by $\theta_{1/2} = 0.33D/h$ independent of the seeing and wavelength of observation.
4. For a screen moving at speed V, the useful integration time for a short-exposure image can be as much as $0.3D/V$ without significant loss in Strehl ratio. The auto-correlation function of the Strehl ratios falls to 0.5 after a time interval $t_{1/2} = 0.26D/V$, independent of the seeing.

Comparison with observations at the NOT shows that the images are a good match to the radial profiles in the simulations and provide rapid methods of measuring the spectrum of turbulence, and give turbulent layer heights of 5−10 km and speeds of translation of about ∼10 m s^{-1}.

The observations show clear evidence of variations in the mean seeing by factors up to ×3 on time-scales from several minutes down to periods as short as 0.2 s and spatial scales of 1 m.

Acknowledgements. We thank David Buscher for his original random screen code and Paul Alexander and Dave Green for extensive and generous help and advice. The Nordic Optical Telescope is operated on the island of La Palma jointly by Denmark, Finland, Iceland, Norway and Sweden in the Spanish Observatorio del Roque de los Muchachos of the Institute de Astrophfisica de Canarias.

References

Baldwin, J. E., Tubbs, R. N., Cox, G. C., et al. 2001, A&A, 368, L1
Buscher, D. 1988, Ph.D. dissertation, University of Cambridge, Getting the most out of COAST
Fried, D. L. 1978, JOSA, 68, 1651
Hecquet, J., & Coupinot, G. 1984, J. Opt., 15, 375
Law, N. M., Mackay, C. D., & Baldwin, J. E., 2006, A&A, 446, 739
Mackay, C. D., Baldwin, J. E., & Tubbs, R. N. 2003, in Proc. SPIE, 4840, 436
Perrin, M. D., Sivaramakrishnan, A., Makidon, R. B., Oppenheimer, B. R., & Graham, J. R. 2003, ApJ, 596, 702
Noll, R. J. 1976, JOSA, 66, 207
Roddier, F., Gilli, J. M., & Vernin, J. 1982, J. Opt., 13, 63
Tubbs, R. N., Baldwin, J. E., Mackay, C. D., & Cox, G. C. 2002, A&A, 387, L21
Wilson, R. W., O'Mahoney, N., Packham, C., & Azzaro, M. 1999, MNRAS, 309, 379